CHAPTER 1
INTRODUCTION

This chapter describes the motivation for doctoral investigation. The contributions and aims of the study are also presented along with a list of project objectives.

1.1 Motivation for the study

Raw sugar produced from sugar cane forms Australia's second largest export crop, contributing four percent of the world's sugar (Anon. 1997). Sugar cane is grown extensively throughout the coastal regions of Queensland and New South Wales, and to a lesser degree in Western Australia. The farming and factory processing of sugar cane is relied heavily upon for economic stability in these regions. The production of raw sugar from sugar cane is basically a two–stage procedure involving processing of the cane stalk to extract the sucrose–rich juice and processing this juice to obtain raw sugar crystal. This investigation is associated with the juice extraction stage of production.

Sugar cane stalks grow to maturity over a period of nine to twenty months and are harvested in Australia between the months of May and November. The harvesting procedure strips the leaf matter from the stalks and cuts them into 200-300 mm long *billets*. In most instances, these billets are collected by haul-out vehicles and delivered to railway sidings for transport to the factory. At the factory, the billets are loaded onto large conveyor belts for delivery to a rotary shredder. The shredder consists of heavy-duty hammers that rotate, creating hammer tip velocities in the vicinity of 100 m/s. Billets of cane are dropped into the rotary shredder and pulverised, producing the process material referred to as *prepared cane*. The nature of sugar cane is such that shredding of the stalk produces a large distribution of particle size in the resulting material. The inner pith material becomes small, relatively soft, highly saturated particles and the rind of the stalk becomes much larger, stronger particles that substantially increase the stiffness of the prepared cane. The prepared cane is conveyed from the rotary shredder to a milling unit where it is formed into a blanket and processed or *crushed* by passing through six circumferentially grooved rollers that are arranged in four counter-rotating pairs. Milling is a high pressure, low temperature process that places the prepared cane under high compressive stress,

hence forcing the extraction of the liquid (sucrose-rich juice and water) from the cane fibre. After the prepared cane has passed though the first milling unit, it is referred to as *first–mill bagasse*. For convenience, the term *bagasse* will often be used in this document when referring to the general milling process material. The first–mill bagasse still contains a significant percentage of sucrose and hence must undergo further processing. Conventionally, a *milling train* of four to six milling units is employed to repeatedly saturate, consolidate and mill the bagasse in order to free and extract the remaining sucrose from the fibre. The bagasse is subsequently termed n^{th}–mill bagasse as it exits the n^{th} mill in the train. Alternatively, extraction of the sucrose via a low pressure, high temperature diffusion process is employed. Diffusion involves the saturation of the bagasse with heated water–sucrose solution, hence leeching further sucrose from the material into the solution. The bagasse leaving the diffuser is saturated and must again be milled in order to reduce its moisture content. Factory efficiency is dependent on the final moisture content of the final mill bagasse, as the material is used as fuel in large boilers to produce steam and often electricity. The sucrose-rich solution that is extracted from the bagasse is collected at the diffuser and/or each mill and cleaned using clarifiers. The clean juice then enters the second stage of processing, involving evaporation and crystallisation processes to produce raw sugar.

The milling of prepared cane and bagasse is thus an important part of raw sugar production. Conventional six–roll milling units are employed nearly exclusively within the Australian sugar industry for milling extraction, and are also used extensively in other sugar producing nations such as Brazil. Milling is an expensive process, as significant power is required to compress the fibrous blanket to the point where no gas or liquid voids are present (hence forcing the extraction of the liquid from the fibre blanket). Advancements in the efficiency and operation of six–roll milling units have historically been the result of trial and error and pilot–scale and factory experimentation.

With the modern introduction of numerical modelling techniques such as the finite element method (Zienkiewicz and Taylor 1989), there has been a strong drive toward simulating the milling process by creating a mill configuration in computer space and implementing mathematical material models to represent the two phases of the bagasse blanket. Knowledge of the process material strength and behaviour offers not only prediction of mill loads and power requirements for existing milling units,

but also provides a platform for simulating changes in mill settings and predicting their effect on power requirements and extraction efficiency. Hence, finite element modelling presents an inexpensive means of determining optimal mill settings and assessing the viability of novel technologies prior to the expensive prototyping process. Prepared cane and bagasse have been identified as a highly compressible semi–saturated fibro–porous material. The flow of the liquid phase (juice) through the material is modelled using Darcy's law for Newtonian flow through permeable material (Bear 1972). The solid phase fibre blanket has been identified to behave in a critical state manner (Britto and Gunn 1989) similar to peat soil (Plaza et al. 2003) and is assumed an isotropic homogeneous continuum during milling. The prediction of bagasse behaviour during milling involves the coupled solution of the governing laws for both phases of the material (Zhao 1993, Owen et al. 1995). The pressure–volume and shear characteristics of the fibre are determined via conventional uniaxial and planar shear experiments (Adam 1997, Plaza et al. 2000) and employed within a candidate critical state constitutive model to create the material yield surface and strain hardening relationship (Anon. 2002). Tests are also conducted on the process material (Adam 1997, Kent and McKenzie 2003) in order to obtain the permeability of the fibre, as a function of the material density. Permeability is the material property describing the ease with which a liquid flows through a porous solid.

Current validation of the predicted behaviour from a calibrated critical state constitutive model has to date consisted entirely of experimental mechanical output. Generally, two–roll milling experiments are conducted, and mechanical quantities such as roll load, torque and speed are recorded. The initial and final liquid contents are also recorded for the material sample. A finite element model of the experiment is subsequently created in computer space using finite element analysis software (Adam 1997, Downing 1999). The calibrated material model is employed in the simulation to represent the porous fibre blanket. The material model for the fibre forms the key element in the solution of the physical event, as it relates the applied stress to the deformation and motion of the blanket in a time iterative procedure, as well as controlling liquid pressures in the sample via fibre permeability. Hence, the material model of the fibre blanket coupled with the liquid flow rule controls the predicted roll reaction forces and moments. These output quantities are concurrent with those taken from the experiment and are thus compared to validate the computational model inputs. Since the first substantial investigation into the finite

element and constitutive modelling of bagasse rolling in 1991 at Swansea (Zhao 1993), predicted load and torque results have improved in relation to corresponding experimental measurements (Adam 1997, Loughran and Kannapiran 2002). The most recent investigations into the development of the critical state fibre model, have resulted in a more fundamental material model for bagasse, based on direct shear (Plaza et al. 2000, Plaza et al. 2002) and refined permeability experiments (Kent and McKenzie 2003). However, torque predictions remain low and the predicted kinematic behaviour is yet to be validated.

Accurate measurement of the kinematics of the fibre blanket for experimental samples offers a means for kinematic validation of predictor models as well as an improved understanding of bagasse behaviour during milling. Furthermore, such knowledge presents the possibility of parameter refinement for critical state models in a reverse finite element procedure. For example, applying the measured strain field to a computational two–roll milling blanket will result in predictions of roll loads and torques, from predicted fibre stresses and liquid pore pressures associated with the forced deformation. These predictions may be compared to experiment values and changes made to relevant constitutive parameters in an iterative manner until the model and experimental outputs correspond. Application of such a procedure to numerous experimental regimes (uniaxial compression, two–roll milling, planar shear, etc.) and across ranges of experimental and material parameters will result in a refined material model that accurately predicts bagasse behaviour over a wide range of loading scenarios.

1.2 Contributions of the study

This study aims to build a significant bridge between bagasse experiments and finite element models. The major contribution of the work will involve the creation and implementation of a numerical image measurement technique for determining the fibre deformation of experimental samples direct from an external material surface, providing accurate output concurrent with that from a finite element model of the experiment.

Experimental apparatus will be designed and implemented to allow visualisation of confined uniaxial compression and two-roll milling experiments for prepared cane and bagasse. Accurate mountings for visual data acquisition will be implemented to allow digital video footage of experiments to be captured. The strain fields

experienced by material samples will be measured directly for series of confined uniaxial compression and two-roll milling experiments. The measured fields of deformation will provide a new method of validation and refinement of the fibre constitutive model and provide insight into the fibre behaviour within experimental samples.

1.3 Aims of the study

In today's competitive marketplace, the Australian sugar industry is dependent upon the efficiency of factory processes. The milling of prepared cane and bagasse is one such process. Developments in milling technology to date have been the result of experimentation and trial and error. Successful mathematical representation of bagasse as a process material is seen as a revolutionary step toward improving process technology at minimal cost. However, the problem is extremely complex due to the organic fibrous nature of bagasse as a process material. The material has lengthy history dependence, a discrete existence at low fibre densities and an evolving fibre size distribution during milling. To date, experimental validation for calibrated bagasse constitutive models has existed in the form of mechanical quantities such as load, torque and liquid extraction.

The main aim of this study is to develop numerical image measurement software capable of mapping solid phase motion and hence deformation on an external 2D surface of a material sample. Software output is to be consistent with that of finite element models in regard to the kinematics and material parameters of the experimental bagasse blankets. This software aims to provide a new method for validation of the material model that is employed to represent the fibrous matrix of bagasse, as well as provide insight to the behaviour of the bagasse fibre at the roll boundary and the development of juice pressure within the blanket.

Coupled with refined experimental procedures, the use of image measurement software will improve the understanding of bagasse behaviour during rolling and groove interactions. Accurately measured deformations will also offer performance assessment of the constitutive model employed to represent the solid phase fibre blanket in finite element milling models. Improved confidence in the modelling of bagasse behaviour will provide a method for low-cost development of both current and new technologies in regard to the extraction of the sucrose-rich juice from the fibrous bagasse blanket.

1.4 Objectives of the study

The primary objectives of this research are:

1. Design and implement experimental apparatus for acquisition of imagery (video footage) of material samples for both confined uniaxial compression and two-roll milling deformation states.
2. Develop a numerical analysis technique for the direct measurement of local material kinematics, from time series of digital images.
3. Apply the developed software to digital imagery taken from series of confined uniaxial compression and two-roll milling experiments in order to measure the deformation experienced by prepared cane and bagasse samples under these loading conditions.
4. Assess the viability of image measurement of prepared cane and bagasse deformations in regard to material homogeneity and numerical considerations.
5. Utilise the measured deformation fields to gain insight into the mechanics of crushing and the development of strains within the fibrous blanket.

CHAPTER 2
RELEVANT KNOWLEDGE AND THEORY

This chapter describes the nature of sugar cane and the industrial processes employed for the extraction of the sucrose–rich juice from the plant stalk. Specific material terminology is defined along with conventional volumetric sugar milling theory. The relevant history of experimental and numerical investigations into the material behaviour and modelling of the milling process is presented and the conventional means of milling experimentation are identified. The mathematics of image displacement measurement with the FFT cross–correlation theorem, continuum kinematics and finite differencing is also presented, as a platform for development of a suitable digital image processing system, for measuring the fibre deformation experienced during bagasse experiments.

2.1 Sugar cane

Sugar cane (Figure 2.1) belongs to a large family of grasses, which contains more than 5,000 species. Included in this family are other economic crops such as barley, rice and wheat. Sugar cane has the ability to trap the sun's energy and convert that energy into sucrose, which is stored as a sweet juice in the stalk of the plant (Anon. 1997).

Figure 2.1. Sugar cane.

Sugar cane stalks are approximately cylindrical in shape and range in diameter from 25–60 mm for mature plants. The hard perimeter of the stalk is known as rind and provides structural strength for the plant and protection of the inner material. The transport function is provided by vascular bundles, which run throughout the cane stalk. A cluster of fibrous sclerenchyma cells surrounds each vascular bundle. The majority of dissolved sugars in the stalk are stored in soft, thin-walled tissue cells called parenchyma. The constituents of the cane stalk can be divided into three categories:

1. Insoluble solids, including storage cell walls, fibrovascular bundles and rind. Insoluble solids constitute 8-18 percent of the stalk mass and are collectively referred to as fibre (Murry 1960).
2. Soluble solids, including the sugars (sucrose, glucose and fructose) and dissolved impurities. Soluble solids constitute 10–16 percent of the stalk mass (Jenkins 1966) and are referred to collectively as brix.
3. Water, which constitutes 73–76 percent of the stalk mass (Jenkins 1966). A portion of the water (25–30 percent of fibre mass) is loosely chemically bonded to the fibre and is referred to as hygroscopic water (Kelly and Rutherford 1957). The term juice is given to the solution of water and soluble solids.

2.1.1 Sugar cane preparation

As part of the harvesting procedure, sugar cane stalks are cut into 20–30 cm long *billets* and loaded into railway transport wagons for delivery to the factory.

Figure 2.2. Billets of sugar cane.

At the factory the cane is transferred onto a conveyor belt and delivered to a rotary hammer shredder. The rotary shredder often consists of heavy-duty tungsten tipped steel hammers that are pivot-mounted on a cylindrical framework. As the shredder rotates, the centripetal motion forces the hammers outward, creating hammer-tip velocities in the vicinity of 100m/s. An adjustable grid-bar is mounted on the inside of the shredder housing and the clearance between the bar and the hammers can be adjusted to vary the *preparation* or *fineness* of the resulting material.

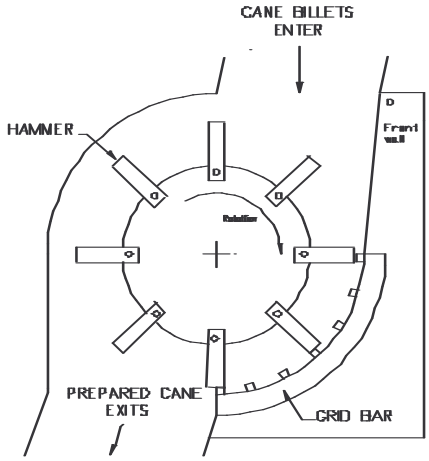

Figure 2.3. Schematic of a typical rotary hammer shredder.

Cane billets are dropped into the shredder and pulverised between the hammer tips and the grid-bar. Shredding of the cane stalk ruptures the storage cells and breaks the rind and fibro-vascular bundles into discrete fibrous particulate. The preparation of the shredded cane is measured in terms of the percentage of ruptured or open cells (POC) in the resulting material (Anon. 1991). The fibrous sponge-like matrix absorbs the free juice that is released from the ruptured storage cells during the shredding process. The product material from the shredding process is referred to synonymously as *prepared* or *shredded* cane.

Figure 2.4. Prepared cane.

The solid constituents of prepared cane can be placed into two distinct categories.

1. Segments of storage cell walls, referred to as *pith* or *fines*. These are less than one millimetre in size and irregular in shape.
2. *Fibres*, resulting from the destruction of the rind and fibro-vascular bundles. These range in size from only a few millimetres in length to fibres 100 millimetres long and up to ten millimetres across.

Prepared cane is thus characterised as a semi-saturated fibro–porous media. However, the fibrous matrix is neither rigid nor completely solid. Both the fines and fibres are organic and are themselves deformable and porous on a microscopic level. In milling theory and material analysis, the solids are assumed to be rigid until there is physically no air or liquid remaining in the material. However, it is noted that the fines have been observed to migrate with the juice flow, through the fibrous matrix.

2.2 Juice extraction

In most sugar factories, prepared cane is initially crushed using a conventional six-roll milling unit, consisting of six circumferentially grooved rolls, ranging 1–1.4 metres in diameter and 1.8–2.7 metres in length. The circumferential grooving on the roll surfaces are generally characterised by groove pitch and angle (Figure 2.5), with 38 mm/35° grooving considered the Australian industry standard. The grooving acts to increase the feeding capacity of the milling unit and has allowed significantly increases in mill throughput (Jenkins 1953, Crawford 1955). The geometric configuration of the six rolls creates four counter-rotating pairs, with each successive

pair having a smaller separation distance or *nip setting* than its previous counterpart. The terms *feed triple* and *delivery triple,* refer the first three and remaining three rolls respectively as shown in Figure 2.5.

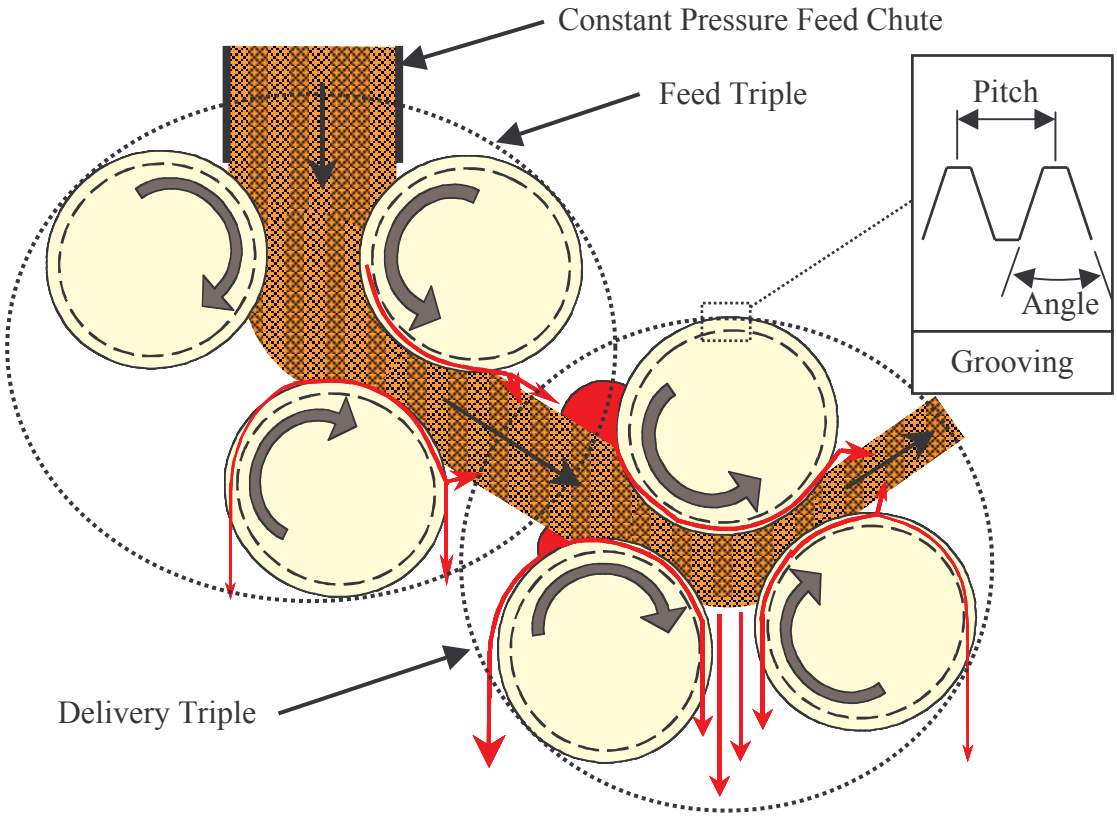

Figure 2.5. Conventional six–roll milling unit.

The prepared cane is formed into a blanket (nominally 500 to 800 millimetres in depth) in the constant pressure feed chute, before passing between the four pairs of counter-rotating rolls. The purpose of the feed triple is to provide sufficient force to feed the material blanket into the delivery triple, where the blanket experiences high levels of compressive stress, and passes through the delivery nip at a blanket depth in the order of tens of millimetres. After the prepared cane has passed through the first milling unit it is termed *bagasse*.

Processing the blanket with one six-roll milling unit does not remove all of the sucrose from the bagasse and so further processing is required. In most factories, bagasse is passed through a milling train, consisting of 4-6 six-roll milling units

(Figure 2.6). The bagasse is rewetted (or macerated) with a hot water/sucrose solution between successive milling units to further dissolve the soluble sugars.

Figure 2.6. Four unit milling train.

Alternatively, the bagasse is placed in a diffuser, where it is saturated with a high temperature solution for the purpose of diffusing the soluble sugars from the cane fibre as shown in Figure 2.7.

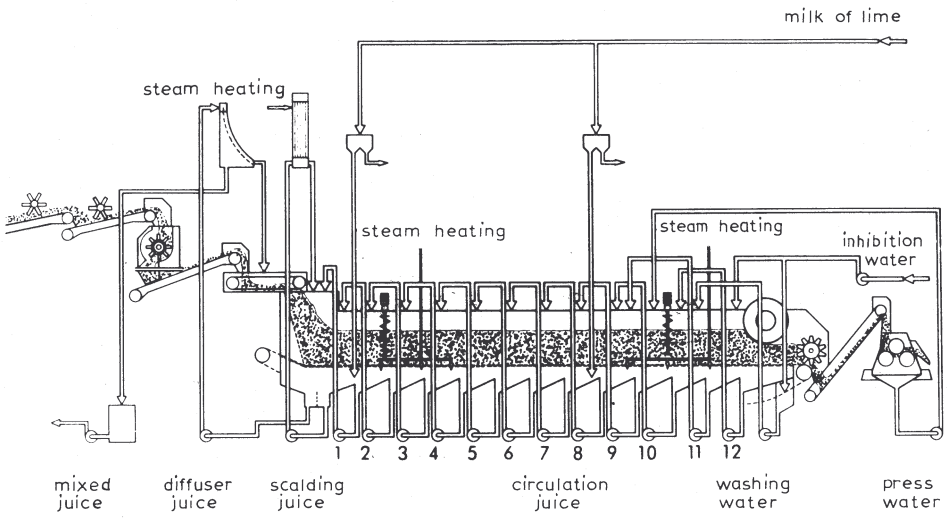

Figure 2.7. The bagasse diffusion process.

Regardless of the intermediate extraction procedure employed, all bagasse is finally *dewatered* with a six-roll milling unit in order to minimise the moisture content of the final bagasse. Reducing the moisture content of final bagasse increases its calorific

value and hence the efficiency of the boilers and co-generation plants which utilise bagasse as a fuel.

Constitutively, bagasse is significantly different to prepared cane. The tips of the roll grooves cut into the blanket surface during milling (Kauppila et al. 2001(2)), continually reducing the physical size of the fibres, as the bagasse passes through the milling train. The fines also lose significant volume during processing, resulting in a very fine, dust–like presence in the bagasse. Bagasse fibre is thus more isotropic than prepared cane fibre because of the reduced average fibre size, and thus exhibits lower shear strength at a given fibre density.

2.3 Sugar cane milling theory

Previous research into the crushing of prepared sugar cane and bagasse has mostly consisted of experimental and theoretical investigations concerning overall material behaviour and prediction of mechanical parameters such as load and torque. Analysis of the crushing of prepared cane and macerated bagasse must consider all three phases of matter in the material. The following figure describes schematically the breakdown of prepared cane into its solid, liquid and gas constituents.

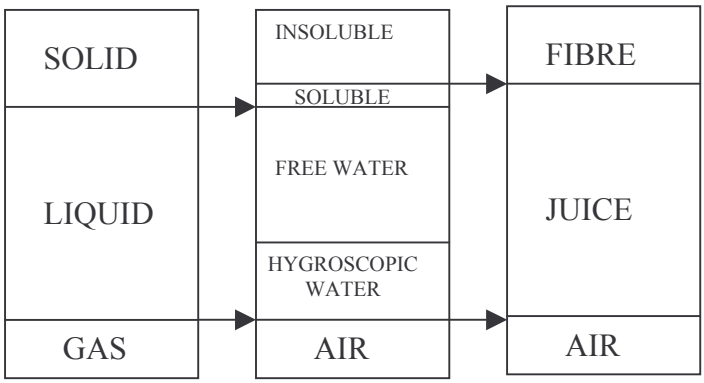

Figure 2.8. The constituents of prepared cane.

Analysis of the compression of prepared cane is performed in terms of the volume of fibre and juice. It is assumed that under the loading conditions considered of interest to milling engineers; the mass and volume of fibre remains constant while the juice volume is separated into expressed juice and juice retained within the fibre. Fibre and juice densities remain constant, but it is evident that the bulk material density will

change due to compression and juice expression. Parameters specific to milling theory are defined in Figure 2.9.

$$Fibre\ \ content\ \ f = \frac{m_f}{m_s\big|_0}$$

$$Fibre\ \ density\ \ \rho_f = \frac{m_f}{V_f} \approx 1530\, kg/m^3$$

$$Juice\ \ density\ \ \rho_j = \frac{m_j}{V_j} \approx 1080\, kg/m^3$$

$$No-gas\ \ volume\ \ V_{ng} = V_f + V_j\big|_0$$

$$No-gas\ \ density\ \ \rho_{ng} = \frac{m_s\big|_0}{V_{ng}} = \left(\frac{f}{\rho_f} + \frac{1-f}{\rho_j}\right)^{-1}$$

$$Compression\ \ ratio\ \ C = \frac{V_{ng}}{V_s}$$

$$Compaction\ \ \gamma = \frac{m_f}{V_s}$$

$$Filling\ \ ratio\ \ C_F = \frac{\gamma}{\rho_f}$$

$$Porosity\ \ n = \frac{V_{voids}}{V_s}$$

$$Void\ \ ratio\ \ e = \frac{n}{1-n}$$

$where:\ \ m - mass$

$V - volume$

$\rho - density$

$f - fibre$

$j - juice$

$s - overall\ \ sample$

$ng - no gas\ \ conditions (juice and fibre only)$

$|_0 - initial\ \ sample\ \ conditions$

Figure 2.9. Material milling parameters.

The mass and volume of the juice that has been extracted from a cane or bagasse sample can be determined by difference, such that:

$$mass\ of\ juice\ extracted\ \ m_{je} = m_j\big|_0 - m_j \qquad \text{(EQ 2.1)}$$

$$volume\ of\ juice\ extracted\ \ V_{je} = V_j\big|_0 - V_j \qquad \text{(EQ 2.2)}$$

Several researchers have identified the crushing of prepared cane and bagasse as a volumetric process that is governed by the geometric configuration and surface speed of the mill rolls (Bullock 1957, Crawford 1957, Murry 1960). Volumetric extraction theory considers the escribed volume rate of a pair of crushing rolls (Figure 2.10), and states that the volume of juice and fibre leaving the mill in unit time should equal this escribed volume.

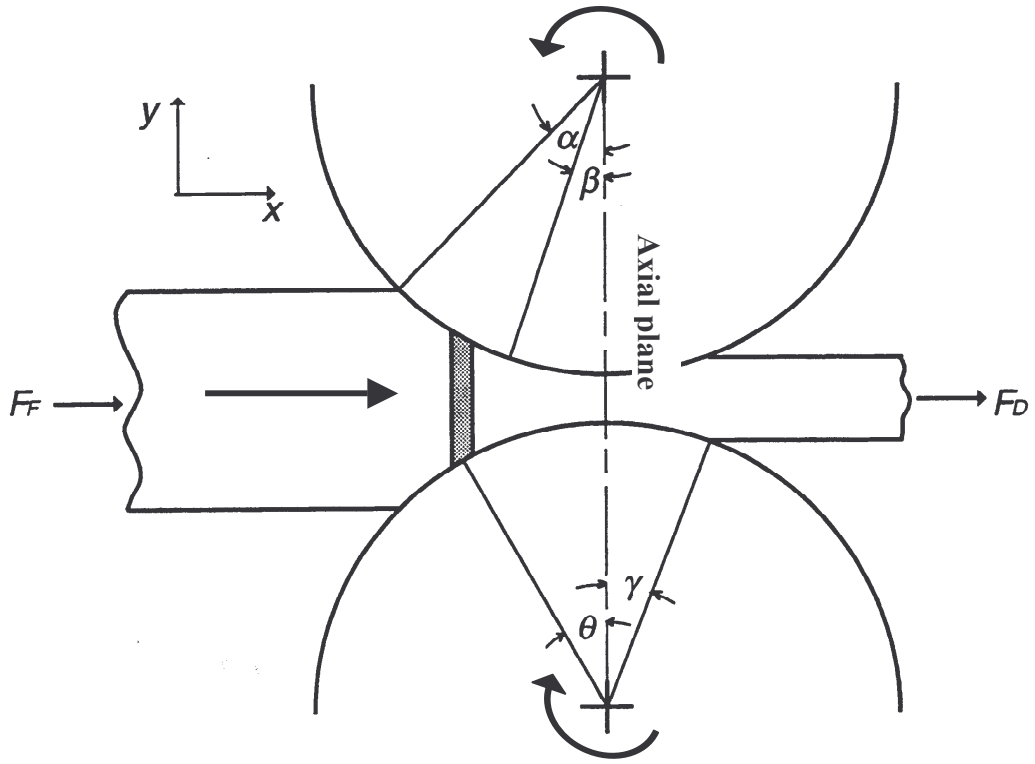

Figure 2.10. Two–roll mill with a shaded element of entering material.

The *contact angle* (α) refers to the roll angle at the initial point of material contact on the roll surfaces. Material is assumed to travel with a horizontal velocity component equal to the roll surface speed (S) multiplied by the cosine of the corresponding roll angle (θ), such that:

$$S_x = S\cos\theta \qquad \text{(EQ 2.3)}$$

Hence, the blanket is assumed to pass the axial plane at the roll surface speed. The escribed volume rate $(\dot{V}_e)$ of the two rolls is expressed as:

$$\dot{V}_e = (W_o L)S \qquad \text{(EQ 2.4)}$$

where (L) is the roll length and (W_o) is the *work opening*, defined as the average distance between the two roll surfaces in the axial plane (Murry and Holt 1967). The volume rate of expressed juice is thus obtained by difference to be:

$$\dot{V}_{je} = \dot{V}_{ng} - \dot{V}_e \qquad \text{(EQ 2.5)}$$

where $(\dot{V}_{ng})$ is the no–gas volume rate of bagasse entering the nip. The theoretical juice extraction for the nip configuration (E_j) is thus determined as the ratio of the expressed juice volume rate to the volume rate of juice entering the mill $(\dot{V}_j)$:

$$E_j = \frac{\dot{V}_{je}}{\dot{V}_j} = \frac{\left(1 - \frac{\dot{V}_e}{\dot{V}_{ng}}\right)}{\left(1 - \frac{\dot{V}_f}{\dot{V}_{ng}}\right)} \qquad \text{(EQ 2.6)}$$

where $(\dot{V}_f)$ refers to the volume rate of fibre entering the mill.

Experimental measurements of the juice extraction for a mill are always less than those predicted from theory (Bullock 1957). A number of possible reasons for this behaviour have been suggested; the most common being that the volume rate of bagasse leaving a roll nip $(\dot{V}_b)$ exceeds the escribed volume rate of the roll pair. The ratio of these two quantities is referred to as the reabsorption factor (k) (Egeter 1928):

$$k = \frac{\dot{V}_b}{\dot{V}_e} \qquad \text{(EQ 2.7)}$$

Following this theory, the volume rate of expressed juice becomes

$$\dot{V}_{je} = \dot{V}_{ng} - \dot{V}_b \qquad \text{(EQ 2.8)}$$

Substitution of EQ 2.7 and EQ 2.8 into EQ 2.6 yields a more representative measure of the juice extraction for a mill:

$$E_j = \frac{\dot{V}_{je}}{\dot{V}_j} = \frac{\left(1 - \frac{k}{C_o}\right)}{\left(1 - f\frac{\rho_{ng}}{\rho_f}\right)} \qquad \text{(EQ 2.9)}$$

where (C_o) refers to the maximum compression ratio of the roll pair.

There is no theoretical prediction for the reabsorption factor, however researchers have developed empirical relations based on available experimental data (Russell 1968, Loughran 1990). Bullock (1957) suggested that the forward slip of bagasse was the major mechanism limiting extraction, and hence referred to the bagasse to escribed volume ratio as the *forward slip factor*. Bullock also conducted extensive two–roll milling experiments, finding that the reabsorption factor increased with increasing compression ratio, with increasing roll speed and with increasing coarseness of preparation. Murry (1960) applied the steel–rolling concept of a neutral plane (Orowan 1943) to the crushing of cane. Assuming that no further juice expression occurred after the neutral plane, he was able to calculate the position of the neutral plane (β) based on the reabsorption factor:

$$\beta = \cos^{-1}\left[\tfrac{1}{2}\left(1 + \frac{W_o}{D}\right) + \sqrt{\tfrac{1}{4}\left(1 + \frac{W_o}{D}\right)^2 - k\frac{W_o}{D}}\right] \qquad \text{(EQ 2.10)}$$

where D refers to the roll diameter. Murry also conducted two-roll milling investigations and confirmed the reabsorption trends of Bullock. Murry's results show that for a given roll surface speed, the reabsorption factor for varying compression ratios converged as the material preparation increased. Furthermore,

Murry's results indicate that the dependence of reabsorption on preparation reduces at lower values of compression ratio. Murry hypothesised that juice may accumulate in paths of low resistance such as the roll grooves, and be carried upward over the bottom roll by groove friction and recombine with the bagasse on the exit side of the roll pair.

Solomon (1967) concluded the dominant mechanism governing reabsorption was the forward extrusion of material through the nip. However, he did state that under conditions different to those used in his experiments, material slip on the roll surface could dominate the reabsorption.

In 1999, researchers at James Cook University School of Engineering conducted an experimental investigation into the effect of mill orientation angle on reabsorption factor (Kauppila and Loughran, 2000). Close to a hundred experiments were conducted on the experimental milling facility at various orientation angles ranging from horizontal to vertical delivery. It was found that mill orientation influenced reabsorption more significantly than compression ratio and roll surface speed. Reabsorption was observed to decrease considerably (20%) with increased mill orientation toward vertical. Results indicated that there was evidence of a threshold orientation for which further rotation toward vertical yielded only a minor decrease in the reabsorption factor. A new empirical equation for reabsorption was determined which includes the influence of mill orientation and also a combined compression-orientation term.

2.4 The mechanics of sugar cane milling

Although the practice of rolling sugar cane to extract juice has been in place for several centuries, it is only during the last 60 years that researchers have developed a scientific understanding of the process. The achievements of Australian researchers in the 1950's and 1960's allowed factories to dramatically increase their crushing rates whilst incurring minimal capital cost (Murry and Holt 1967). In more recent times, advances have been made in developing complex, fully coupled computational models of the rolling process (Zhao 1993, Owen et al. 1994, Owen et al. 1995, Adam 1997, Owen et al. 1998, Loughran and Adam 1998, Plaza et al. 2002, Loughran and Kannapiran 2002). This section summarises the contributions of numerous researchers, past and present, to the field of crushing mechanics.

2.4.1 Experimental investigations

It is suggested (Murry 1960) that the first investigation into the mechanics of cane crushing was conducted by Deerr (1912). Deerr developed a pressure-volume relationship for the fibrous matrix through compression tests performed on prepared cane and bagasse using a drained cylindrical test cell. Deerr noticed that juice expression under a given pressure increased with the fineness of preparation, and also that more expression occurred as the blanket thickness decreased. It was also found that the pressure-volume behaviour of dry fibre was very different to that of prepared cane or bagasse.

Atherton (1954) performed more compression tests, again employing a cylindrical drained test cell. Four levels of cane preparation were used, and the brix of the expressed juice was measured. Atherton showed that the brix decreased with increasing pressure; indicating that high-brix juice was easily expressed under low pressure, but low-brix juice required more energy for expression.

Pidduck (1955) determined the density, Poisson's ratio and Young's modulus for both wet and dry fibre under high pressure. Blankets were compressed in a cylindrical cell, allowing time for juice pressure to dissipate. Pidduck's results showed that the ratio of radial to axial pressure for quasi-static loaded wet fibre (0.60) was almost twice that of dry fibre (0.365). It was also noted that dynamic loading of the wet fibre again increased the value to (0.76); and that loading rate had no effect on the ratio for dry fibre. The elastic constants for the dry fibre were calculated as; Young's modulus = 8250 MPa, bulk modulus = 6700 MPa, Poisson's ratio = 0.3. It should be noted that these values are determined under very high pressures, and thus refer to the bulk phase of the material and not the overall behaviour of the fibrous matrix.

Bullock (1957) commenced the University of Queensland's cane crushing investigation with his doctoral thesis, investigating the physical properties of prepared cane and bagasse. Bullock confirmed the applicability of Deerr's pressure-volume relation, through further press tests, and found that the results were significantly affected by preparation level and apparatus capabilities. Density and equivalent elastic constants were measured experimentally to be: Young's modulus = 6700 MPa; bulk modulus = 4900 MPa; Poisson's ratio = 0.27. The permeability of prepared cane was measured using both direct flow and consolidation techniques. In an attempt to simulate mill crushing, dynamic press tests were performed, and the methodology for controlled two-roll milling experiments documented. The effects of compression

ratio, roll speed, preparation and blanket thickness were studied using the experimental two-roll mill. For the first time, Bullock's capacity number (C_N) was established as a valuable milling parameter and is a dimensionless measure of crushing rate per unit roll speed. A frictional theory for mill feeding was established and validated from friction coefficients determined from feed pressures and directly measured friction coefficients.

Murry's doctoral thesis (Murry 1960) documents major experimental and theoretical advances made in the understanding of cane crushing. Two-roll mill results are reported for a wide range of milling conditions. Load, torque and juice extractions are presented along with pressure pin measurements taken via a one-eighth inch diameter pin mounted on the roll surface. The torque-load number (N) was introduced and is an expression depicting the relationship between roll load and torque. Murry also conducted a series of dynamic confined uniaxial compression tests in a rectangular test cell. Auxiliary investigations measured juice viscosity, permeability and values of the friction coefficient for prepared cane on steel.

Holt (1963) conducted experimental investigations associated with load prediction in the crushing process. A porous-walled flow cell was used to determine both axial and transverse permeability of prepared cane over a range of compression ratios. Confined and unconfined uniaxial compression tests were also conducted using Murry's test cell. Unconfined tests showed small amounts of lateral extrusion and also that the cane blankets did not penetrate to the root of the grooves.

Cullen (1965) documents an experimental investigation of the shear and frictional behaviour of bagasse. Uniaxial and triaxial shear tests were conducted, despite the limitations of ram travel and capacity for the triaxial shear apparatus. Friction and internal shear coefficients were determined and documented for a range of experimental conditions.

Murry and Holt (1967) used experimental two-roll data and theoretical considerations to investigate the factors that primarily influence roll load. With other conditions unchanged, it was found that the roll load was directly proportional to both compression ratio and roll diameter.

Solomon (1967) performed experiments to measure the horizontal component of roll load, pressure-compression characteristics of cane at low pressures and the conditions required for mill feeding on the two-roll experimental mill. A load measuring segment was set into the surface of the roll and used to measure both radial and

tangential loads experienced during crushing. Pressure tappings measured local hydraulic pressure at various locations from root to tip of the grooves. Solomon also conducted rolling experiments using flat rolls and made comparison with grooved roll experiments at the same compression ratios. A two–dimensional finite difference solution for juice flow was performed based on Darcy's law, and determined over the domain via finite difference techniques. This analysis was conducted as a means for roll load prediction and results compared well to experimental roll loads. The solution however required knowledge of the position β of the neutral plane, which limited the scope of predictions for the model.

Russell's doctoral thesis (Russell, 1968) contains several experimental investigations. For the purpose of his feeding studies, Russell determined the pressure-compression characteristics of prepared cane and bagasse at low pressures. A pressure probe was used in the blankets for two-roll milling experiments in order to measure juice pressure in the blanket centre. The pressure distributions from the probe were integrated and compared well with the roll load measured at the bearing blocks on the two-roll mill. Using the roll load proportionality expressions (Murry and Holt, 1967), Russell developed an empirical relationship for roll load as a function of filling ratio and roll diameter.

Loughran's doctoral thesis (Loughran, 1990) presents experimental investigations into the confined dynamic and quasi-static compression of prepared cane, using Murry's rectangular test cell. A new measure for assessment of cane preparation was developed based on precompressor results, and is referred to as the treatment number. Treatment number is statistically independent of fibre content and decreases with increased preparation. Loughran developed three separate empirical equations for test cell platen force, based on Holt's dynamic compression tests, Loughran's dynamic compression tests and Loughran's quasi-static compression tests. All three equations relate the platen force to coefficients of the compression ratio, treatment number and platen speed. Two-roll mill and mill feeding experiments were also performed along with the associated precompressor measurements. Loughran developed an empirical equation for roll load in terms of roll diameter, roll surface speed, compression ratio and the treatment number. This relationship was based on the experimental two-roll data of Bullock (1957) and Murry (1960). An empirical equation was also developed for the reabsorption factor (k) in terms of the compression ratio, roll surface speed and

the treatment number. The Loughran regression equations gave better fit to the experimental data than previous empirical models.

Leitch (1996) studied the triaxial compression of prepared cane. Drained triaxial tests were performed for a single cane variety and preparation at both low and high pressure. The fibrous matrix demonstrated anisotropic behaviour under hydrostatic loading conditions, as well as the elastic recovery of the material upon unloading. Leitch provides regression equations to fit observed behaviour in terms of logarithmic elastic and plastic moduli of the material.

Adam (Adam 1997) conducted an extensive program of dynamic uniaxial compression tests using a rectangular test cell with the same geometry as the cell used by Murry and other researchers mentioned above. Adam used multiple groove geometries, finding that in most cases the material did not fully penetrate the grooves of the platens. The juice pressure distribution was measured with partial success and pressure in the blanket centre was found to increase with increased compression ratio. Energy considerations were examined in the context of energy required for a set extraction. A theoretical minimum energy required was determined by conducting material compression tests between flat porous platens, and this was found to be one third of the energy required for the same extraction using grooved platens with a groove angle of 55^0. Sinusoidal compression tests were also conducted as a better representation of the compression experienced during rolling. It was found that for this advanced loading technique, the peak juice pressure occurred before the minimum work opening, indicating further evidence of a neutral plane as introduced by Murry (1960). Adam also conducted quasi-static uniaxial compression tests for the purpose of calibration of constitutive models for use in computational modelling of bagasse behaviour. The constitutive modelling conducted by Adam is discussed in the following section.

Downing (1999) conducted both uniaxial compression and rolling experiments as part of his doctoral investigation into the effects of soil contamination on the crushing of prepared cane. It was found that soil contamination significantly increased the stiffness response of prepared cane under both quasi-static and dynamic uniaxial compression. By sinusoidal loading of specimens, Downing found that the prepared cane relaxes as a result of pore pressure abatement and secondary effects, including solid reordering and hydraulic conduction of juice through un-ruptured cell walls due to internal cell pressure. Relaxation is therefore believed to contribute to the

reduction in peak juice pressure prior to completion of the compression stroke (and prior to the axial plane during rolling). The reduction in void ratio of the material due to the introduction of soil was found to reduce the permeability of prepared cane. Thin blanket rolling experiments conducted on the JCU two-roll advanced milling facility yielded an equation relating roll load and groove geometry to fibre stress. Downing states that further testing on blanket thicknesses leading to positive set between the grooved rolls is likely to be more informative than the thin blanket tests conducted which are not of direct significance to factory crushing at present.

In 2000, uniaxial compression tests were performed using a rectangular test cell of the same cross-section used by Murry and others (Kauppila et al. 2001(1)). The cell was modified for increased drainage performance and increased sample capacity. This was an important step toward understanding the response behaviour of cane and bagasse in the factory by allowing the blanket height to approach that of factory crushing rates. It was found that large blanket height, large angled grooving and low compression speed returned consistently lower moisture content. Two distinctive failure mechanisms were identified at the groove-cane interface and the bridging factor was introduced as a method for failure mode prediction based on sample mass and groove pitch (Kauppila et al. 2001(2)). Success of large angle grooving is due to higher volumetric deformation. Shear deformation is unproductive for extraction because energy is consumed with no decrease in local blanket volume.

2.4.2 Computational modelling of cane and bagasse milling

Loughran (1990) was the first to apply the finite element method (Bathe 1996) for solution of the juice velocity and pressure distributions in the nip region of two crushing rolls. Loughran applied the solution technique to solve over a two–dimensional domain corresponding to that used by Solomon (1967) for the finite difference solution of the same juice flow problem. Based on the flow theory (Darcy's law with advection) and assumptions made by Solomon, the finite element method was employed to solve the two–dimensional partial differential equations introduced by Solomon in his doctoral thesis (Solomon 1967); for both solid and porous roll surface boundary conditions. The solution, as was the case in Solomon's work, was a single-phase (liquid) solution and did not consider the presence of the solid fibre matrix. Loughran's finite element solutions were in strong agreement with the finite difference solutions presented earlier by Solomon.

Zhao (1993) was the first to investigate the application of multiphase porous media mechanics to the rolling of prepared cane. Zhao employed the finite element method to solve the fully coupled unsaturated-saturated two–phase flow problem, and implemented linear (elastic and elasto-plastic) and non-linear (elastic and rigid plastic) hardening models for the solid phase fibres (Owen et al. 1995). Both steady–state and transient solution schemes were written and implemented. Results were obtained for the mentioned constitutive models over the region of interest for two-roll crushing. It was found that a stress-strain relationship of exponential form gave the best load and pressure predictions. As a result of this, Zhao developed an inverse finite element procedure and determined a distinct constitutive equation based on compression in a uniaxial test cell. This equation was employed for further uniaxial and rolling finite element simulations, resulting in more accurate load and pressure prediction over a limited range of conditions. This research identified the definite advantages of constitutive based finite element modelling and also the need for a more practical constitutive model for bagasse. The implementation of sophisticated adaptive meshing routines, resulting in more robust numerical simulations for the rolling of coupled multi–phase materials.

In 1997, a document was prepared for the Sugar Research Development Corporation SRDC (Leitch et al. 1997), in which available isotropic and anisotropic constitutive models were assessed for use in numerical cane modelling. It was stated that available anisotropic models were too complex for employment by available finite element codes. Leitch recommended a modified isotropic crushable foam model akin to (Anon. 2002) for the solid phase.

Adam's doctoral thesis (Adam 1997) contains an extensive investigation into the applications of current porous media constitutive models to the uniaxial compression and rolling of prepared cane and bagasse. Linear and non-linear elasticity models were coupled with isotropic porous media plasticity models (crushable foam, modified cam-clay and capped Drucker-Prager). No anisotropic models were investigated. Compression and rolling simulations were conducted, with modifications to important constitutive parameters (primarily the slope (M) of the critical state line), yielding closer representation of material behaviour and experimental load and torque results (Loughran and Adam, 1998). Adam identified the Capped Drucker-Prager constitutive model with modified permeability response and adjusted critical state slope (M value of 3.8) to be the most appropriate model

available for prepared cane. The high value of the critical state slope was not directly measured from the material, but rather determined by correlating the lateral extrusion in the numerical solution with measurements from unconfined (one side plate removed) uniaxial experiments. This was considered a novel method of representing the inherent anisotropy of bagasse that results from the large particle size distribution and layering of these fibres during compression.

Comparison of simulation results with Murry's two-roll experimental results and Loughran's empirical roll load equation showed that levels of roll load and torque were consistently lower than experiment (approximately 20-30% for load and 50% for torque). Trends of roll load with other parameters were however all in good agreement with experiment indicating that simulation is capable of representing the mechanics of milling. Analysis of predicted blanket velocities in the nip region indicated that forward slip, shear and juice flow relative to fibre were all evident, but not sufficiently to account for the observed levels of excess bagasse volume. Predicted trends of juice extraction and reabsorption with compression ratio, roll surface speed and roll diameter all showed good agreement with experiment.

Comparison of predicted and measured pressure distributions on the roll surface and within the blanket indicated that while predicted levels are low, predicted and measured distributions are very similar in form.

Downing employed the modified capped Drucker-Prager model developed by Adam for simulation of the rolling of soil-contaminated cane (Downing 1999) as part of his doctoral investigations. While extensive simulation was conducted, only minor changes were made to parameters governing the operation of the constitutive model.

Plaza (Plaza et al. 2000) conducted direct shear tests on bagasse using apparatus true to the method of soil shearing analysis (Britto and Gunn 1989), in pursuit of a more fundamentally driven critical state model (Plaza et al. 2002). Results returned (M) values for bagasse that were more concurrent with those from soils literature (M = 1.0–1.2). Bagasse was documented to behave in a similar fashion to peat soils (Plaza et al. 2003), and milling simulations using the direct shear results showed representative fibre behaviour.

2.4.3 Summary of findings

The benefits resulting from crushing mechanics research over the past 60 years are evident in the improved performance of Australian (and overseas) sugar factories. The development of volumetric theory and a macroscopic understanding of the effects of varying key crushing parameters has allowed crushing rates to increase ten-fold. Millers are now able to more accurately predict roll loads, roll torques and other performance indicators through the application of empirical models.

Recent research efforts have been directed toward the numerical simulation of the rolling process. The current state-of-the-art utilises a fully coupled flow through porous media formulation to model what is assumed to be an isotropic continuum–based problem. To advance significantly in this area it is becoming increasingly apparent that a more detailed understanding of the material physical behaviour is required. The behavioural influences of non-homogeneities including particle size distribution, non-uniform void distribution, non-uniform feed saturation, and planar fibre layering need to be defined. The complexity associated with roller grooving and its influence on the boundary conditions of the rolling process is also a considerable obstacle. The acquisition of digital imagery from various two–roll milling and uniaxial compression experiments offers qualitative visualisation of bagasse behaviour during rolling and groove interactions. Furthermore, customised application of numerical image displacement measurement will provide quantitative measurement of the deformation experienced by the fibre blanket, hence providing a new method of model validation and finetuning.

2.5 Digital image processing systems

In the last 30 years, image processing systems have become widely utilised as a means for data acquisition and event visualisation. For example, the knowledge and capacity of the medical industry has significantly advanced through the use of X–rays and various other image scanning techniques. Closer to this work, the image displacement and velocity measurement of particle seeding, has significantly improved the understanding of Newtonian fluid flow, within complex geometries (Buchhave 1992, Hopkins et al. 2000). From the beginning, when image displacements were measured using completely optical techniques

(Raffel et al. 1998), to the computational method of direct measurement from digital images (Willert and Gharib 1991), particle image velocimetry has held a strong presence in the field of fluid mechanics. However, only recently has this methodology found its way into the field of solid–phase mechanics (Lueptow 2000, White et al. 2001(1&2)).

A modern digital image processing system (Figure 2.11) consists of a light source, a sensor system (commonly a CCD camera) and an interface between the sensor system and the host computer. The primary operation of the interface or frame grabbing hardware is to convert CCD analog output and store it in RAM as digital data that the host computer can interpret.

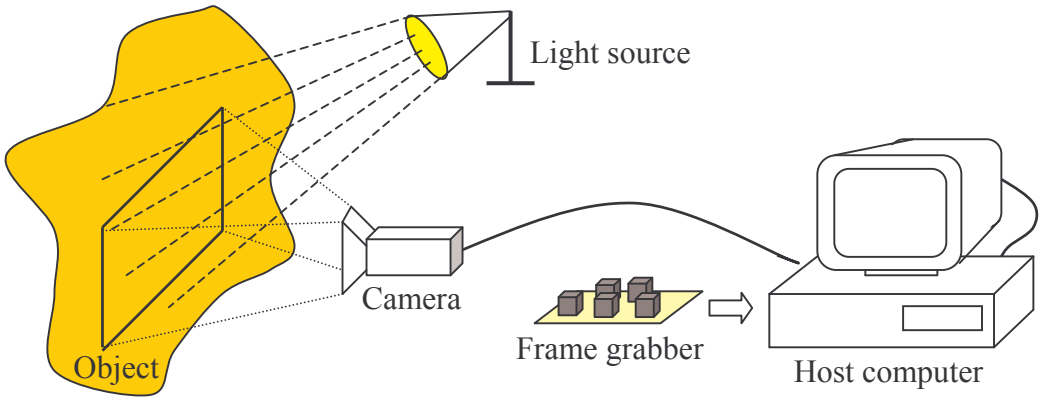

Figure 2.11. A typical digital image processing system.

2.5.1 Lighting

The correct choice of light source is vital for image processing success and must be chosen to suit the system environment. Quality illumination provides the basis for quality imagery and hence reduces the need for image restoration. The aim of the light source is to produce a homogeneous and time-constant illumination field over the entire subject. A list of the possible light sources and their suitable applications in contained in Appendix A.

The placement of the light source in relation to the subject is equally as critical as the source itself. The resulting images are strongly influenced by the position of the light source. The four methods of lighting a subject are detailed in Appendix A.

2.5.2 CCD cameras

A Charged Coupled Device (CCD) consists of light-sensitive semi-conductors called pixels. These pixels are generally arranged to form a matrix with a horizontal to vertical ratio of 4:3 (CCD area scan cameras). The CCD sensor is the most important component of a digital camera. The quality of the CCD sensor/s used in a digital camera governs the resolution and colour accuracy of the resulting images. The physics of a CCD sensor is described by the inner photo effect (Jansen 1993). Incoming photons produce electrons in the semi-conductor material. The quantity of freed electrons is proportional to the amount or intensity of the light that falls on the sensor. These electrons are separated in the photo diode and are stored in a capacitor. The capacitor is connected via a metal–oxide semi–conductor (MOS) transistor, to a surrounding electrical circuit (Roulston 1999). The MOS transistor acts as a light switch; when it is open, the charges are collected in the capacitor and when the switch closes the electrons are transported. The principal methods of integrating pixel information into a serial data stream are detailed in Appendix A.

CCD chips are available in various sizes and are characterised by *tube diameter*. The term tube diameter refers to the diameter of the circle that is required for sufficient light to reach all the CCD pixels. For example, a tube diameter of 1" has a rectangular active window (4:3) measuring just less than 16 mm diagonally. Standard CCD chip sizes range in tube diameter from 1/4" to 1". With modern emphasis on size minimisation, 1" CCD chips are nowadays rarely used, with most applications employing smaller chips (1/4", 1/3"and 1/2"). Corresponding physical pixel sizes range between 4μm x 4μm (1/4" CCD chip) and 16μm x 16μm (1" CCD chip) (Graf 1997). CCD cameras are available in a vast range of configurations, depending on the desired application. The range of the electro-magnetic spectrum that a camera is sensitive to depends on the CCD semi-conductor material. As discussed above, incoming photons of light lift electrons from the valence band to the conduction band of the semi–conductor material, hence creating free charge transport. The number of electrons that are freed from any given pixel in the CCD sensor is proportional to the number of incoming light photons that fall on that pixel. The spectral range and sensitivity of a CCD sensor is hence governed by the energy gap between the valence and conduction bands of the semi-conductor material employed in the CCD chip. For a semi-conductor of known energy gap, the upper limit of wavelength visible to the

CCD chip can be calculated (Schwinger 1998). CCD cameras for application in the visible light spectrum employ gallium-alloy or cadmium-alloy semi-conductors and are sensitive to light in the wavelength range of 400–1000 nm.

2.5.3 Camera lenses

In order to control the depth of field and the amount of light that falls on the CCD sensor/s, a lens must be fitted to the camera. A camera lens consists of a system of mirrors and lenses and at least one aperture. The depth of field and the amount of light that enters the lens are controlled by the size of the aperture and the time that it is open to incoming light (exposure time). The geometric principles of a lens are detailed in Appendix A. In order to standardise lenses for all sizes of CCD chips, the term normal lens is given to a lens with a photographic angle of 45° for a CCD chip size equivalent to the frame size of 35 mm camera film. This selection of 'normal' lens geometry results in a focal length of approximately 50 mm. Lenses with photographic angles larger than 45° are referred to as *wide- angle lenses*. Lenses with a smaller photographic angle than 45° are termed *tele-photo lenses*. The term *zoom lens* is given to a lens that possesses the ability to vary its focal length and show a focussed image for a range of object distances.

2.5.4 Frame grabbing hardware

The primary objectives of the frame grabber hardware within a digital image processing system are to interpret the electrical voltage signal produced by the CCD sensor/s and store this information as digital images that can be displayed on a host computer. In modern digital image processing systems, the frame grabber hardware can either be located onboard the camera or as a hardware card within the host computer. In the context of digital image processing, the three basic components of a frame grabber system are the *video input unit*, the *frame buffer* and an array of *digital signal processors* DSP. When analog output is required, a video output unit is also required to convert the digital signal to analog for storage on a VHS cassette.

The video input unit VIU provides the interface between the CCD sensors and the digital image storage unit or frame buffer. The VIU must perform the following tasks:

- *Mutiplex the input data sources*: In many cases the image data consists of more than one channel of video signals, such as the red, green and blue channels from a three CCD colour camera. High performance frame grabbing hardware possesses the ability to interpret and process multi-channel signals in parallel. Alternatively, a multiplexing unit is incorporated, which selects and processes one signal channel at a time. However, for the system to switch between the multiple input signals, they require external synchronisation by the host computer clock or a *sync generator*.
- *Synchronise the incoming video signals*: In situations where a multiplexing unit is employed within the frame grabber hardware, synchronised separation is incorporated in order to correctly interpret the incoming analog signals. The horizontal and vertical sync signals are extracted from the input data so that each data line within an image and each image field can be identified and produced at the correct time within the signal. Hence, sync separation can be thought of as a switch between the different input signals that control the spatial and temporal image layout.
- *Digitise the analog input signal*: An analog to digital (AD) converter is used to produce a digital representation of the CCD signal. The standard resolution of AD converters is 8-bit. However, variable scan systems incorporate AD converters with the ability to change their frequency, allowing input signals other than the norm to be processed.
- *Provide a digital interface*: Some modern cameras have onboard AD converters and hence provide a digital input signal to the VIU. Hence a parallel or serial interface must be provided to allow this digital input signal to bypass the AD converter.

The digital image data produced by the VIU can be stored either in the *frame buffer* of the frame grabber hardware or in the host computer storage. With the introduction of modern data transfer hardware such as the IEEE1394 Fire-wire card and increased computer storage space, data transfer rates are sufficiently high to allow direct storage of the digital image data on the host-computer. Alternatively, the data is stored in the frame buffer of the frame-grabber hardware. The frame buffer is a RAM area that is configured to store the image data in layers of x-y matrices, the number of which

corresponds to the resolution of the AD converter (i.e. 8 layers for an 8-bit AD converter). An array of *digital signal processors (DSP)* is sometimes incorporated in frame grabber hardware to perform image-processing algorithms such as image convolutions, filters and data compression. Hence the DSPs create digital image files from the digital image data, in a file format (e.g. TIFF- tagged image file format) that is compatible with post-processing software.

2.6 Numerical Image displacement measurement using the FFT cross–correlation method

Numerical two–dimensional image displacement measurement using the direct Fast Fourier Transform (FFT) spatial cross–correlation is a procedure most commonly employed within particle image velocimetry (PIV) software (Buchhave 1992). The procedure allows determination of the average two-dimensional displacement of a region within a digital image, and hence the instantaneous velocity of the region. Consider the pair of sequential digital time images as shown in Figure 2.12.

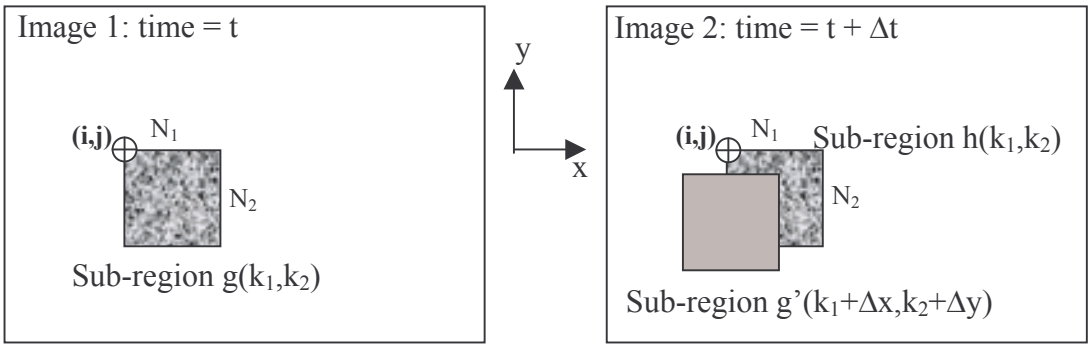

Figure 2.12. Sub-regions within sequential time images.

Here we explain the determination of the displacement of the N_1 x N_2 pixel sub–region, or spatial pixel intensity function $g(k_1,k_2)$, over the time increment (Δt). For optimal FFT computation, the pixel dimensions (N_1, N_2) of the sub–regions (g and h) should be equal to an integer power of two, and each other. The two–dimensional discrete Fourier transforms for the spatial pixel intensity functions, $g(k_1,k_2)$ and $h(k_1,k_2)$, can be described by the complex functions $G(n_1,n_2)$ and $H(n_1,n_2)$ over the same spatial domain, such that:

$$G(n_1,n_2) \equiv \sum_{k_2=1}^{N_2} \sum_{k_1=1}^{N_1} \exp(2\pi i k_2 n_2 / N_2) \exp(2\pi i k_1 n_1 / N_1) \quad \text{(EQ 2.11)}$$

$$H(n_1,n_2) \equiv \sum_{k_2=1}^{N_2} \sum_{k_1=1}^{N_1} \exp(2\pi i k_2 n_2 / N_2) \exp(2\pi i k_1 n_1 / N_1) \quad \text{(EQ 2.12)}$$

The direct cross–correlation theorem (Raffel et al. 1998) states that the cross–correlation of two functions is equivalent to the multiplication of the discrete Fourier transform of the time (t) sub–region $g(k_1,k_2)$ with the complex conjugate of the Fourier transform of the time (t+Δt) sub–region $h(k_1,k_2)$. Hence:

$$Corr(g(k_1,k_2),h(k_1,k_2)) \Leftrightarrow G(n_1,n_2)H^*(n_1,n_2) \quad \text{(EQ 2.13)}$$

where * represents the complex conjugate and $G(n_1,n_2)$ and $H(n_1,n_2)$ are real functions such that $H(-n_1,-n_2) = H^*(n_1,n_2)$. The inverse Fourier transform of the complex conjugate multiplication is calculated to produce the actual cross-correlation plane, which has the same spatial dimensions (N_1 x N_2) as the input sub–region functions. For a finite two-dimensional pixel displacement (Δx,Δy), the cross–correlation plane displays a *peak* or best match of the two sub–region spatial functions at some (k_1,k_2) location in the cross-correlation plane (Figure 2.13).

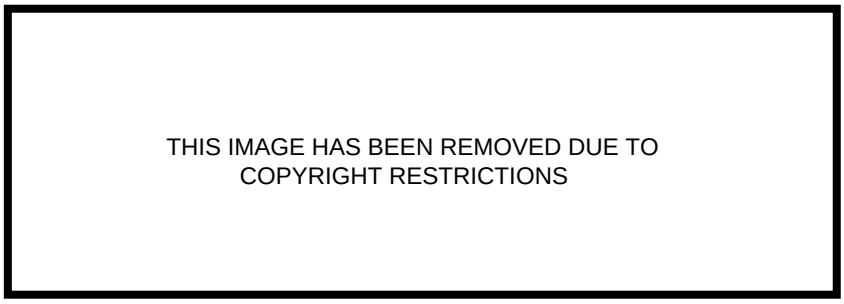

Figure 2.13. Example of the peak in the cross–correlation plane (Westerweel 1993).

For the purpose of image displacement measurement, such a peak defines the two–dimensional pixel displacement of the sub-region $g(k_1,k_2)$ during the time interval Δt, to single pixel accuracy.

The application of two-dimensional FFT's for determination of the cross-correlation plane has a number of associated numerical and experimental issues that must be considered.

1. *Sample sizes:* The FFT computational efficiency is primarily determined by repeated application of a symmetry property between the even and odd discrete Fourier transform coefficients (Brigham 1974). The most common and efficient FFT algorithms require input data (sub-region functions) to have dimensions of 2^n (i.e. 16 pixel x 16 pixel or 32 x 32 pixel sub–regions). Other FFT algorithms exist (radix-4, radix-3, split-radix FFT) but their computational complexity often fails to justify their implementation.
2. *Data period:* The Fourier transform by definition, is an integral over the domain extending from negative infinity to positive infinity. However, in practice the integrals are computed over finite spatial domains (sub–regions). Such domain sampling is justified by assuming the data to be periodic or continually repetitive in all directions. This assumption of data periodicity presents two issues for consideration (Raffel et al. 1998):
    a. *Aliasing:* Due to the assumed periodicity of the input sub-region functions, the resulting cross-correlation data is itself periodic. Hence, if the two-dimensional cross-correlation data of length (N, N) contains a displacement signal larger than half of the sub–region size (N/2), the correlation peak is affected by the data periodicity and will appear on the opposite side of the correlation plane. That is, for a true displacement $U_{true}>N/2$, the measured displacement will be $U_{meas} = U_{true}– N$. The solution to this problem is to either increase the sub–region sample size or preferably to reduce the time interval (Δt) between images or exposures.
    b. *Bias Error:* As sub–region displacement (or shift) increases, fewer pixel intensity values are actually correlated with each other, resulting in an underestimation of displacement. For example, at a shift of half the sub–region dimension (N/2) only half of the two sub–regions being

correlated are overlapping and hence correlation plane data must be weighted accordingly. For the case of cross-correlation between two sub–regions of equal size, the correlation plane has a triangular weighting distribution. The weighting at the sub–region centre (zero shift) is always unity, as complete correlation between the sub–regions will occur. The weighting diminishes linearly with distance from the centre of the correlation plane to a value of 0.5 at the correlation plane boundaries. Bias errors can be neglected for pixel shifts less than one–quarter of the sub–region side length (Westerweel 1993).

3. *Calculation of the correlation coefficient:* The correlation coefficient is a measure of the coincidence between the two sub–region pixel intensity functions (g and h) and is thus calculated for all possible (k_1,k_2) positions within the sub–region. The correlation coefficient is evaluated as follows:

$$c_{gh}(k_1,k_2)=\frac{\sum_i\sum_j\left[g(i,j)-\bar{g}\right]\times\left[h(i+k_1,j+k_2)-\bar{h}(k_1,k_2)\right]}{\sqrt{\sum_i\sum_j\left[g(i,j)-\bar{g}\right]^2\times\sum_i\sum_j\left[h(i+k_1,j+k_2)-\bar{h}(k_1,k_2)\right]^2}} \quad \text{(EQ 2.14)}$$

where summation is applied over the entire (k_1,k_2) sub–region. The value $\bar{g}$ is the average of the correlation plane and need only be computed once. The value $\bar{h}(k_1,k_2)$ is the average of $h(k_1,k_2)$ coincident with the template g at the position (k_1,k_2) and hence must be determined for all (k_1,k_2) positions. The maximum value of the correlation coefficient for the sub–region is determined and utilised to identify the (k_1,k_2) pixel location of the correlation peak. The magnitude of the maximum correlation coefficient $c_{gh}(k_1,k_2)$ provides a means for comparing particle–tracking success between different sub–regions within an image pair, or different image pairs within the image series.

4. *Displacement peak estimation to sub–pixel accuracy:* Sub-pixel accuracy can be achieved when estimating the location of the displacement peak in the cross–correlation plane. The cross correlation data can be utilised to increase the accuracy of the displacement estimation by investigating the gradients of the data surrounding the whole-pixel displacement estimate. This is commonly achieved by fitting a function to the correlation data. Generally,

the two adjoining pixels are used in each direction to fit a function to the data surrounding the correlation value of interest. Such techniques are often referred to as three-point estimators (Raffel et al. 1998). The most common three-point estimations are the parabolic and Gaussian peak fits. The parabolic fit is blunt and is most suitable for images involving low contrast and particles of irregular shape. The Gaussian fit estimates a sharper peak that is more commonly the case in PIV analyses involving high levels of contrast and seed particles of uniform shape.

5. *Image contrast:* In traditional fluid-flow applications of the FFT correlation, laser imaging is used to illuminate seeding particles in the flow to produce image samples. The resulting exposures have distinctive contrast in that the grey-scale pixel intensities of the particles are far separated from those of the flow or image background. This study presents the application of the FFT cross–correlation to measuring displacement of locations within bagasse blankets. It has not been shown in the literature that bagasse, in a natural or seeded state, can provide the required contrast for successful image displacement measurement using the direct FFT cross–correlation.
6. *Displacement gradients:* Error in measured displacements can arise from significant displacement gradients (or deformation) of the material over the time interval between sequential time images. As deformation occurs, the pixel pattern within each sub–region changes, making statistical matching of the sub–region functions more difficult. The solution to this problem is to minimise the time increment between image samples and/or the time rate of the experiment.

2.7 Continuum kinematics

This section presents the classical theory of continuum mechanics in regard to the kinematics of historic continua. The theory of continuum mechanics is the basis for solution of material motions and stresses in a finite element solver. Following Truesdell (Truesdell 1966), the three primitive elements of continuum mechanics are bodies, motions and forces. The theory of bodies and motion will be concentrated upon here, as it is the motion of the fibre blanket under external and internal loads that we wish to describe.

2.7.1 Bodies and motions

A body (ß) is considered as a set of particles, or body points, denoted here by **X**. In continuum mechanics, the body is assumed to be smooth. This infers that the body occupies a single uninterrupted domain in Euclidean space. Hence, the group of particles **X**, can each be given an identity. That is, the location of each particle within the set **X**, can be represented with respect to an origin (**O**) by three real numbers (X^1, X^2, X^3), often referred to as the *intrinsic coordinates* (X^α) of the particle. The mapping of the body to a domain is assumed continuously differentiable. The body (ß) is also assumed to have a non-negative mass distribution $M(p)$ defined over a σ-ring of subsets (p), the parts of the body.

Bodies are physically available only in their configurations, or open regions in Euclidean space that they occupy at some point in time. Configurations are not to be mistaken for the bodies themselves, but can be considered as mappings of the body (ß) in Euclidean space. The *motion* of the body (ß) is the time series or *history* of its configurations, and is described by the deformation function $(\tilde{\chi})$:

$$\tilde{x} = \tilde{\chi}(X, t) \qquad \text{(EQ 2.15)}$$

where (X) is a particle, (t) is some point in time ($-\infty < t < \infty$) and $(\tilde{x})$ is the location of the particle (X) in Euclidean space at time (t), with reference to the origin (**O**). Hence, the deformation function $(\tilde{\chi})$ contains the locations of the set of body points (**X)** at all available times. Motions are smooth, only if the deformation function is differentiable with respect to time, as many times as is required. Hence, the common definitions of velocity and acceleration hold:

$$\dot{\tilde{x}} = \frac{\partial}{\partial t}\tilde{\chi}(X, t) \qquad \text{(EQ 2.16)}$$

$$\ddot{\tilde{x}} = \frac{\partial^2}{\partial t}\tilde{\chi}(X, t) \qquad \text{(EQ 2.17)}$$

2.7.2 Mass density

We have established that the body (ß) is a continuum as it occupies an uninterrupted domain in Euclidean space. The mass distribution $M(p)$ however, will be left arbitrary and is thus determined as the volume integral of particle density:

$$M(p) = \int_V \rho_X dv \qquad \text{(EQ 2.18)}$$

The mass density provides a relationship between the body (ß) and the configuration that it occupies at any point in time.

2.7.3 Reference configuration

It is often convenient, especially in solid mechanics, to select one possible configuration $(\widetilde{\kappa})$ as a reference for (ß). Thus the mapping,

$$\widetilde{X}_{\widetilde{\kappa}} = \widetilde{\kappa}(\mathbf{X}) \qquad \text{(EQ 2.19)}$$

provides the positions $(\widetilde{X}_{\widetilde{\kappa}})$ of the body particles (**X**) in the reference configuration $(\widetilde{\kappa})$. By assumption this reference mapping is smooth, hence $\widetilde{\kappa}$ is invertible, such that

$$\mathbf{X} = \widetilde{\kappa}^{-1}(\widetilde{X}_{\widetilde{\kappa}}) \qquad \text{(EQ 2.20)}$$

The selection of $(\widetilde{\kappa})$ is arbitrary and need not be a configuration that the body will ever occupy, only a possible one. Hence there are an infinite number of possible reference configurations, each of which provides a unique description of a given motion. Thus the relationship,

$$\widetilde{x} = \widetilde{\chi}[\widetilde{\kappa}^{-1}(\widetilde{X}_{\widetilde{\kappa}}), t] \equiv \widetilde{\chi}_{\widetilde{\kappa}}(\widetilde{X}_{\widetilde{\kappa}}, t) \qquad \text{(EQ 2.21)}$$

describes the motion as a sequence of mappings, of the reference configuration $(\widetilde{\kappa})$ onto the actual configurations $(\widetilde{\chi})$ of the body.

2.7.4 Descriptions of motion

Consider a general (scalar, vector or tensor) time dependent spatial field (ϕ) that is defined over the deformable body (ß). In the *material description*, the independent variables are the particles (X) and the time (t). Hence its material description can be expressed as

$$\phi(X,t) = \phi(\tilde{\chi}(X,t),t) \qquad \text{(EQ 2.22)}$$

The term *Lagrangian* or *referential* is given to the material description when a reference configuration is employed. The referential description is the most commonly used in modern solid mechanics.

In the *spatial description* of the spatial field (ϕ), attention is given to the current configuration of the body (ß), or the region of Euclidean space occupied by the body at the present time (t). The spatial description is often termed the *Eulerian description* and takes the current position $(\tilde{x})$ of the particles and the time (t) as independent variables. Since the motion is invertible, the spatial field $\phi(X,t)$ can be replaced by a function of $(\tilde{x})$ and time:

$$\phi(X,t) = \phi[\tilde{\chi}^{-1}(\tilde{x},t),t] \equiv \Phi(\tilde{x},t) \qquad \text{(EQ 2.23)}$$

Here, the function (Φ) is unique. Hence, whilst there are an infinite number of referential descriptions of a motion, there is only one spatial description. Thus, in the spatial description, attention is focused on a fixed region of space over the time period of the motion. The spatial description is most suited to analysis of fluids, which involve rapidly deforming masses and large relative particle motions.

2.7.5 The deformation gradient

The deformation gradient $(\tilde{F})$ is the gradient of a referential motion,

$$\tilde{F} \equiv \tilde{F}_{\tilde{\kappa}}(\tilde{X},t) = \nabla\tilde{\chi}_{\tilde{\kappa}}(\tilde{X},t) \qquad \text{(EQ 2.24)}$$

and provides the linear approximation to the mapping $(\widetilde{\chi}_{\widetilde{\kappa}})$, or the gradient of the deformation from $(\widetilde{\kappa})$ to $(\widetilde{\chi})$. Thus the concept of a deformation gradient presumes the presence of a defined reference configuration $(\widetilde{\kappa})$. If we define the independent curvilinear coordinates (X^{α}) and (X^{m}) in the reference and current configurations respectively, the referential motion can be described as:

$$\widetilde{x}^{m} = \widetilde{\chi}^{m}_{\widetilde{\kappa}}(X^{1}, X^{2}, X^{3}); m = 1,2,3 \qquad \text{(EQ 2.25)}$$

Hence, the components of the deformation gradient tensor are the nine partial derivatives of the three functions $(\widetilde{\chi}^{m}_{\widetilde{\kappa}})$ with respect to the reference coordinates (X^{α}) and are expressed in component form as:

$$\widetilde{F}^{m}_{\alpha} = \widetilde{x}^{m}{}_{,\alpha} \equiv {}^{\partial}X_{\alpha}[\widetilde{\chi}^{m}_{\widetilde{\kappa}}(X^{1}, X^{2}, X^{3}, t); m = 1,2,3; \alpha = 1,2,3 \qquad \text{(EQ 2.26)}$$

The determinant of the deformation gradient is often referred to as the Jacobian, and provides a measure of local density per unit density in the reference configuration. Hence,

$$J = \left|\det \widetilde{F}\right| \ \textit{and} \ \ \rho_{\widetilde{\chi}} J = \rho_{\widetilde{\kappa}} \qquad \text{(EQ 2.27)}$$

where $(\rho_{\widetilde{\chi}})$ and $(\rho_{\widetilde{\kappa}})$ denote the mass densities in the present and reference configurations respectively.

2.7.6 Cauchy's polar decomposition

The deformation gradient tensor $(\widetilde{F})$ is non-singular, due to the inherent assumption of smooth motions. Therefore, it may be written in two forms according to Cauchy's polar decomposition theorem (Lai et al. 1974):

$$\widetilde{F} = \widetilde{R}\widetilde{U} = \widetilde{V}\widetilde{R} \qquad \text{(EQ 2.28)}$$

Here, the rotation tensor $(\widetilde{R})$ is orthogonal, such that $\widetilde{R}\widetilde{R}^T = \widetilde{I}$ and $\det \widetilde{R} = \pm 1$. The positive-definite symmetric tensors $(\widetilde{U})$ and $(\widetilde{V})$ are the right and left stretch tensors respectively. Hence the deformation corresponding to $(\widetilde{F})$ can be thought of as pure stretches (λ_i) along three suitable orthogonal axes $(\widetilde{N}_i)$, followed by a rigid rotation of these axes onto the orthogonal axes $(\widetilde{n}_i)$. Alternatively, by performing the rigid rotation between $(\widetilde{N}_i)$ and $(\widetilde{n}_i)$ first and then effect the same pure stretches (λ_i) along $(\widetilde{n}_i)$. The right and left stretch tensors are most easily obtained via the right $(\widetilde{C})$ and left $(\widetilde{B})$ Cauchy-Green tensors and the deformation gradient. Hence,

$$\widetilde{U} = \sqrt{\widetilde{C}} = \sqrt{\widetilde{F}^T \widetilde{F}} \qquad \text{(EQ 2.29)}$$

$$\widetilde{V} = \sqrt{\widetilde{B}} = \sqrt{\widetilde{F}\widetilde{F}^T} \qquad \text{(EQ 2.30)}$$

Because $(\widetilde{C})$ and $(\widetilde{B})$ are symmetric, it is possible to determine their eigenvalues $(\lambda_i^{\,2})$ and corresponding eigenvectors and rewrite their expressions as:

$$\widetilde{C} = \sum_{i=1}^{3} \lambda_i^{\,2} \widetilde{N}_i \otimes \widetilde{N}_i \qquad \text{(EQ 2.31)}$$

$$\widetilde{B} = \sum_{i=1}^{3} \lambda_i^{\,2} \widetilde{n}_i \otimes \widetilde{n}_i \qquad \text{(EQ 2.32)}$$

The right and left stretch tensors are thus constructed as follows:

$$\widetilde{U} = \sum_{i=1}^{3} \lambda_i \widetilde{N}_i \otimes \widetilde{N}_i \qquad \text{(EQ 2.33)}$$

$$\widetilde{V} = \sum_{i=1}^{3} \lambda_i \widetilde{n}_i \otimes \widetilde{n}_i \qquad \text{(EQ 2.34)}$$

where (λ_i) are the *principal stretches* and $(\widetilde{N}_i)$ and $(\widetilde{n}_i)$ are the unit eigenvectors of $(\widetilde{C})$ and $(\widetilde{B})$, or $(\widetilde{U})$ and $(\widetilde{V})$ respectively. By continuity,

$$\det \widetilde{U} = \det \widetilde{V} = \left| \det \widetilde{F} \right| = J \qquad \text{(EQ 2.35)}$$

2.7.7 Finite strain measures

The *Doyle-Erickson* family of Lagrangian finite strain tensors are expressed with the general equation:

$$\widetilde{\varepsilon}^{m} = \begin{cases} \frac{1}{m}(\widetilde{U}^{m} - \widetilde{I}) & m \neq 0 \\ \ln(\widetilde{U}) & m = 0 \end{cases} \qquad \text{(EQ 2.36)}$$

where (m) is a real number and $(\ln \widetilde{U})$ denotes the tensor logarithm of $(\widetilde{U})$. The better–known members of this family are the Green–Lagrange strain $(m = 2)$, the Almansi strain $(m = -2)$, the Biot or nominal strain $(m = 1)$ and the Hencky or logarithmic strain $(m = 0)$.

2.7.8 Velocity gradient, rate of deformation and spin tensors

The velocity gradient tensor $(\widetilde{L})$ is defined as the spatial gradient of velocity (Anon. 2002), and is conveniently described in terms of the deformation gradient as follows:

$$\widetilde{L} = \dot{\widetilde{F}}\widetilde{F}^{-1} \qquad \text{(EQ 2.37)}$$

The velocity gradient can be shown to be the sum of its symmetric and skew components, such that:

$$\widetilde{L} = \dot{\widetilde{\varepsilon}} + \widetilde{\Omega} \qquad \text{(EQ 2.38)}$$

where $(\dot{\widetilde{\varepsilon}})$ is the symmetric rate of strain tensor, defined as

$$\dot{\widetilde{\varepsilon}} = \frac{1}{2}\left(\widetilde{L} + \widetilde{L}^{T}\right) \qquad \text{(EQ 2.39)}$$

and $(\widetilde{\Omega})$ is the skew spin tensor, defined as

$$\widetilde{\Omega} = \frac{1}{2}\left(\widetilde{L} - \widetilde{L}^{T}\right) \qquad \text{(EQ 2.40)}$$

This breakdown of the velocity gradient tensor can thus provide a deeper understanding of a mapped body motion. Time rates of stretch and rotation provide insight into the nature of a motion, beyond that provided by instantaneous finite strain measures.

2.8 Finite difference approximations for first derivatives

Finite differencing (Levy and Lessman 1959) provides a computationally inexpensive method of approximating the spatial and temporal derivatives of motion that form the deformation gradient and the time rate tensors.

2.8.1 Taylor series expansions

Taylor series expansions are often used to generate such approximations (Kreyszig 1988). Consider the referential motion $\tilde{\chi}(\tilde{X},t)$ of a simple one–dimensional mapping of a body shown in the space–time grid in Figure 2.14.

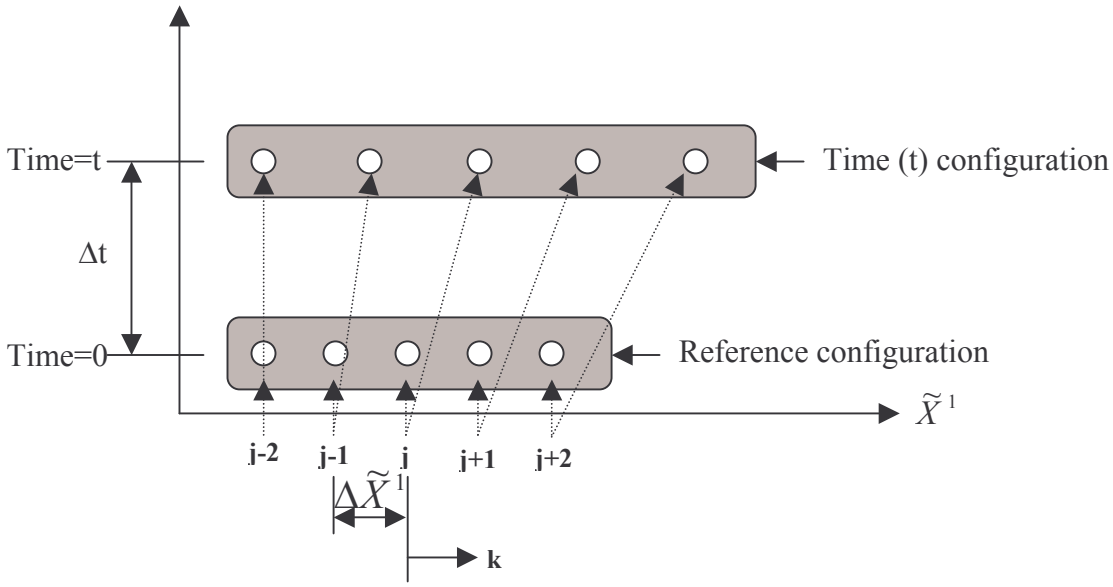

Figure 2.14. Space–time grid showing the reference and time (t) mappings of the referential motion $\tilde{\chi}_{\tilde{\kappa}}(\tilde{X},t)$.

The general Taylor series for the motion $\tilde{\chi}_{(j+k)}$ at the particle $(j+k)$ is expressed as:

$$\tilde{\chi}_{(j+k)} = \tilde{\chi}_{(j)} + (k\Delta X^1)\left(\frac{\partial\tilde{\chi}}{\partial X^1}\right)_j + \frac{1}{2}(k\Delta X^1)^2\left(\frac{\partial^2\tilde{\chi}}{\partial X^{1^2}}\right)_j + .. + \frac{1}{n!}(k\Delta X^1)^n\left(\frac{\partial^n\tilde{\chi}}{\partial X^{1^n}}\right)_j + .. \qquad \text{(EQ 2.41)}$$

where $k = \pm 1, \pm 2, \cdots$ and the time is fixed. Consider the Taylor series expansion for $\tilde{\chi}_{(j+1)}$ at the point (j+1):

$$\tilde{\chi}_{(j+1)} = \tilde{\chi}_{(j)} + (\Delta X^1)\left(\frac{\partial \tilde{\chi}}{\partial X^1}\right)_j + \frac{1}{2}(\Delta X^1)^2\left(\frac{\partial^2 \tilde{\chi}}{\partial X^{1^2}}\right)_j + .. + \frac{1}{n!}(\Delta X^1)^n\left(\frac{\partial^n \tilde{\chi}}{\partial X^{1^n}}\right)_j + .. \quad \text{(EQ 2.42)}$$

Subtracting $\tilde{\chi}_j$ and dividing throughout by ΔX^1 yields the first-order approximation for $\left(\frac{\partial \tilde{\chi}}{\partial X^1}\right)_j$:

$$\frac{\tilde{\chi}_{(j+1)} - \tilde{\chi}_{(j)}}{\Delta X^1} = \left(\frac{\partial \tilde{\chi}}{\partial X^1}\right)_j + \frac{1}{2}(\Delta X^1)\left(\frac{\partial^2 \tilde{\chi}}{\partial X^{1^2}}\right)_j + .. \quad \text{(EQ 2.43)}$$

Hence, the expression $\frac{\tilde{\chi}_{(j+1)} - \tilde{\chi}_{(j)}}{\Delta X^1}$ provides an accurate approximation for the first spatial derivative $\left(\frac{\partial \tilde{\chi}}{\partial X^1}\right)_j$, only if ΔX^1 is relatively small compared to some pertinent length scale. However, consideration of the space difference $\frac{\tilde{\chi}_{(j+1)} - \tilde{\chi}_{(j-1)}}{2\Delta X^1}$ provides a second-order approximation of $\left(\frac{\partial \tilde{\chi}}{\partial X^1}\right)_j$ with higher accuracy. Thus,

$$\frac{\tilde{\chi}_{(j+1)} - \tilde{\chi}_{(j-1)}}{2\Delta X^1} - \left(\frac{\partial \tilde{\chi}}{\partial X^1}\right)_j = \frac{1}{6}(\Delta X^1)^2\left(\frac{\partial^3 \tilde{\chi}}{\partial X^{1^3}}\right)_j + \frac{1}{120}(\Delta X^1)^4\left(\frac{\partial^5 \tilde{\chi}}{\partial X^{1^5}}\right)_j + .. \quad \text{(EQ 2.44)}$$

This second-order approximation is termed the *three-point centred* difference approximation, and is often seen in the form

$$\left(\frac{\partial \tilde{\chi}}{\partial X^1}\right)_j = \frac{\tilde{\chi}_{(j+1)} - \tilde{\chi}_{(j-1)}}{2\Delta X^1} + O(\Delta X^1)^2 \quad \text{(EQ 2.45)}$$

where $O(\Delta X^1)^2$ is the residual error associated with the approximation.

2.8.2 Point difference operators

Second order point difference operators provide an approximation to the first derivative at one discrete point in a spatial or temporal grid, in terms of the

surrounding grid points. The three-point centred difference approximation presented in the previous section can provide such an approximation for any point in a grid that is not located on the grid boundary.

Second order three-point operators also exist for approximating the first derivative at points that lie on the boundary of a mesh. These approximations, termed *three-point forward* and *three-point backward* approximations utilise the spatial locations of the point of interest and the two adjacent points to approximate the derivative. The weightings in the formulation of the forward and backward approximations are such that they carry the same level of error as the three-point centred approximation. Thus, the forward and backward three-point approximations are respectively expressed as

$$\left(\frac{\partial \tilde{\chi}}{\partial X^1}\right)_j = \frac{-3\tilde{\chi}_{(j)} + 4\tilde{\chi}_{(j+1)} - \tilde{\chi}_{(j+2)}}{2\Delta X^1} + O(\Delta X^1)^2 \qquad \text{(EQ 2.46)}$$

$$\left(\frac{\partial \tilde{\chi}}{\partial X^1}\right)_j = \frac{\tilde{\chi}_{(j-2)} - 4\tilde{\chi}_{(j-1)} + 3\tilde{\chi}_{(j)}}{2\Delta X^1} + O(\Delta X^1)^2 \qquad \text{(EQ 2.47)}$$

The finite point-difference operators presented here provide a suitable method for approximating the spatial and temporal derivatives of motion that form the components of the deformation gradient and the time rate tensors.

2.9 Summary

The material and process theory of bagasse milling was presented and the relevant experimental and computational research history reviewed, identifying appropriate means of bagasse experimentation (two–roll milling, uniaxial compression and direct shear methods). A description of modern digital image processing systems was presented and the major components of such a system are detailed in Appendix A. Numerical image displacement measurement with the FFT direct correlation algorithm and the theory of continuum kinematics was presented, along with suitable finite difference techniques for approximation of the first spatial and temporal derivatives of motion. Hence, this chapter has created the platform for development of a suitable image processing system for measuring the two–dimensional deformation of external surfaces of bagasse samples.